ACS APPLIED MATERIALS & INTERFACES

Research Article

Cite This: ACS Appl. Mater. Interfaces 2019, 11, 32310−32319

www.acsami.org

Assembling Metal−Organic Frameworks into the Fractal Scale for Sweat Sensing

Zhengyun Wang, Ting Liu, Lipei Jiang, Muhammad Asif, Xiaoyu Qiu, Yang Yu, Fei Xiao, and Hongfang Liu*

Key Laboratory of Material Chemistry for Energy Conversion and Storage, Ministry of Education, Hubei Key Laboratory of Material Chemistry and Service Failure, School of Chemistry and Chemical Engineering, Huazhong University of Science and Technology, Wuhan 430074, P. R. China

Supporting Information

ABSTRACT: Many natural organizations with some special functional properties possess fractal tissues which display nearly the same at every scale. The benefit of mimicking fractal structure in synthetic functional materials warrants further exploration. To tackle this challenge, we assemble metal−organic frameworks (MOFs) into fractal structures by using a bottom-up approach inspired from evaporation-driven crystallization. Such hierarchically branched MOFs exhibit some unexpected performances in electrochemistry, and can be a versatile biosensor for sweat analysis. Our work provides an interesting and efficient example for fabricating fractal MOFs as well as uncovering their new properties. This fractal-guided strategy can be extended to synthesize and explore new characteristics of other materials, holding potential in various applications including sensors, catalysis, and energy storage.

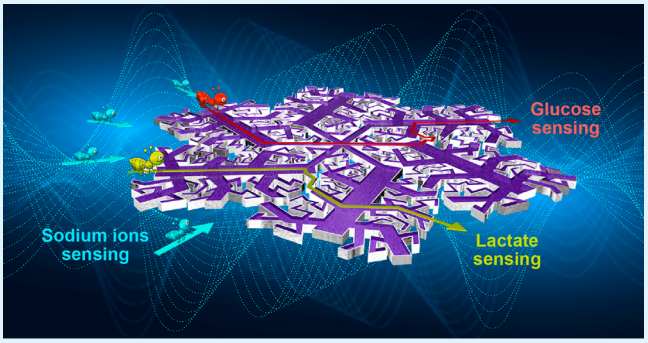

KEYWORDS: *fractal MOFs, self-similar, random walk, self-assembly, sweat sensing*

INTRODUCTION

Natural systems not only are able to create self-similar structures spanning over multiple scales, but also possess exceptional capabilities of evolution, self-regulation, and acclimatization.[1−3] For example, human lungs follow the pattern of repeated tree-shaped bifurcation in order to fully absorb oxygen in a limited volume.[4] The surface of the human brain shows self-similar lines, which ensures a larger surface area in the finite volume and further endows us with more complex thinking ability.[5] Beyond these, the urinary system, distribution of neurons, double helix DNA structure, and even molecular chains of proteins all feature self-similarity, that is, the same at every scale of magnification. This category of self-similar structures is referred to as fractals, which defines a mathematical set describing self-similar patterns with non-integer dimensions.[6] Many inanimate objects such as ice crystals, lightning, mountain ranges, and canyons and some prototypical patterns in geometry including Koch curve, Cantor set, and Sierpiński triangle also have fractal structures. These elegant and fascinating fractal patterns characterized by self-organization, self-similarity, and irregularity as well as the underlying principles have been introduced into diverse fields including art, geomorphology, physics, chemistry, biology, and economics.[7−12] However, in materials science, although some fractal related research has been reported,[13,14] the beneficial effect of fractal on the functional properties of materials deserves further exploration, especially for the areas of applied functional materials design. As a matter of fact, inspired from nature or life all along, human activities and societal advancements have extensively benefitted from natural and manufactured materials.[15−18] Among these materials, metal−organic frameworks (MOFs), composed of periodical organic linkers and inorganic metal ions/clusters, have emerged and attracted tremendous interest in diverse applications from catalysis, gas storage and separation, sensors to energy storage and conversion.[19−22] Also, the physicochemical properties of MOFs would be influenced by their synthesis approaches, forms, orientation, distributions, sizes, and morphologies in different scales.[23−25] It is interesting to propose more special considerations for concerning the emergence of new properties of MOFs at fractal scale. From the mathematical theory of fractals, the fractal pattern is limited in area but infinite in circumference. In other words, the surface area of finite space formed by fractal MOFs is infinite. It is envisioned that the introduction of the fractal concept into the design of MOFs would dramatically regulate their edge, active areas, and other properties and further launch a new direction in the field of materials science.

Based on the above description, a thought-provoking question spontaneously arises: How can the MOFs be

Received: July 4, 2019
Accepted: August 14, 2019
Published: August 14, 2019

DOI: 10.1021/acsami.9b11726
ACS Appl. Mater. Interfaces 2019, 11, 32310−32319

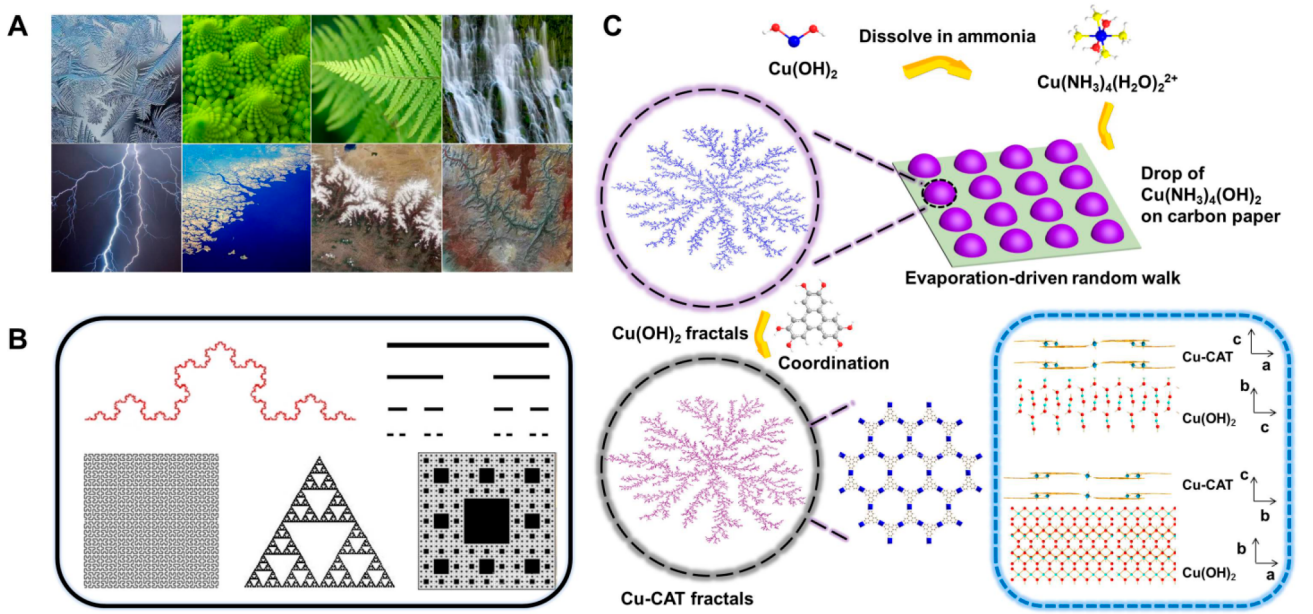

Figure 1. (A) Fractal patterns (from left to right and top to bottom) in nature: ice crystals, Rome cauliflower, fern, waterfall, lightning, coastline, mountain range and canyon. (B) in geometry: Koch curve, Cantor set, Peano curve, Sierpiński triangle and cube. (C) Preparation process of Cu-CAT fractals.

assembled into fractal structures? Current efficient approaches including layer-by-layer deposition,[26] electrochemical manufacturing,[27] hydrothermal preparation,[28] microwave synthesis,[29] monolayer self-assembly,[30] and gel-layer techniques[31] have been devoted to fabricate various MOFs crystals. However, given the complicated relationship between the precise coordination and resulting morphology, it is unpredictable for the MOFs construction of fractal architectures with hierarchical branches to use these conventional methods. The way toward forming of MOF fractals seems to face bottlenecks. Consequently, we need to convert thought and draw inspiration from another angle. Picture this scene: what will be observed after a drop of salt water slowly dries on the table? It leaves uniform branched and self-similar "trees" pattern through diffusion limited aggregation (DLA).[32] We speculate that it is highly desirable to self-assemble MOFs in the fractal scale by using this slow evaporation driven way. Although MOFs are insoluble in solvents, we might as well seek its soluble precursor to dissolve and recrystallize to achieve a fractal precursor as a staring template, and further realize the oriented conversion of MOFs through lattice match.

Herein we propose a "fractal MOFs" concept that fabricates MOFs with self-similar branched structure. A facile approach inspired from brine evaporation has been used to self-assemble MOFs into the fractal scale, as displayed in Figure 1. In our approach, $Cu(OH)_2$ as the precursor was first dissolved in dilute ammonia−water and then recrystallized on carbon paper (CP) to form $Cu(OH)_2$ fractals used for subsequent generation of the Cu-catecholate (Cu-CAT) MOF fractals. One discovery is that our large-area MOF fractals would form via a two-step self-assembly: evaporation-driven random walk and heteroepitaxial growth. Moreover, some unexpected properties of MOFs are discovered, which is in favor of sweat sensing applications. Wearable sweat biosensors as a type of burgeoning smart electronics would give individuals insight into disease diagnosis, health assessment, and personalized care in the near future.[33−35] Sweat contains abundant chemical information that could potentially indicate the deeper biomolecular state of testers. Sweat sodium ions (10−100 mM) would provide early warning for muscle cramps, dehydration, and hyponatremia;[36] sweat glucose (10−200 μM) has been proved to be closely related to blood glucose (4−8 mM), which could be considered for treatment of glycometabolism related disease;[37] sweat lactate (5−20 mM) as a pressure ischemia biomarker is able to reflect insufficient oxidative metabolism as well as tissue viability compromise.[38] However, development of current wearable sweat biosensors based on noble metals and enzyme is restricted to the high cost and stability of the sensing element. Therefore, the long-term vision is to explore materials with multiple sensing ability and superb performances as well as low cost, stability, and facile synthesis methods. Interestingly, CP/Cu-CAT fractals can measure sodium ions effectively due to the edge effect. Also, the subdiffusion endows the CP/Cu-CAT fractals with the capability to detect glucose in acid media, whereas for glucose sensing copper-based catalysts will not operate in acidic sweat due to its limited oxidation. The as-prepared CP/Cu-CAT spanning fractal dimensions exhibit outstanding sensing performances toward sodium ions, glucose, and lactate, which could be a versatile electrochemical biosensor for real human perspiration monitoring. We also expect that the proposed fractal guided strategy will pave a novel avenue for discovering and extending more functions of MOFs or other materials in extensive applications.

EXPERIMENTAL SECTION

Synthesis of CP/Cu-CAT Fractals. Conventional carbon paper (CP) was tailored to a small size (1 cm × 1 cm) as the light, conductive, and freestanding substrate for supporting the fractals MOFs. For $Cu(OH)_2$ precursor fabrication, 0.5 M NaOH (5 mL) was prepared and added dropwise into 0.25 M $Cu(NO_3)_2$ (5 mL) with stirring for 5 min. The obtained light-blue product was centrifuged and then carefully washed five times to achieve pure $Cu(OH)_2$ after drying. Next, the $Cu(OH)_2$ powders were put into prepared 0.1 M $NH_3{\cdot}H_2O$ solution. $Cu(OH)_2$ will coordinate to NH_3 and dissolve in

DOI: 10.1021/acsami.9b11726
ACS Appl. Mater. Interfaces 2019, 11, 32310−32319

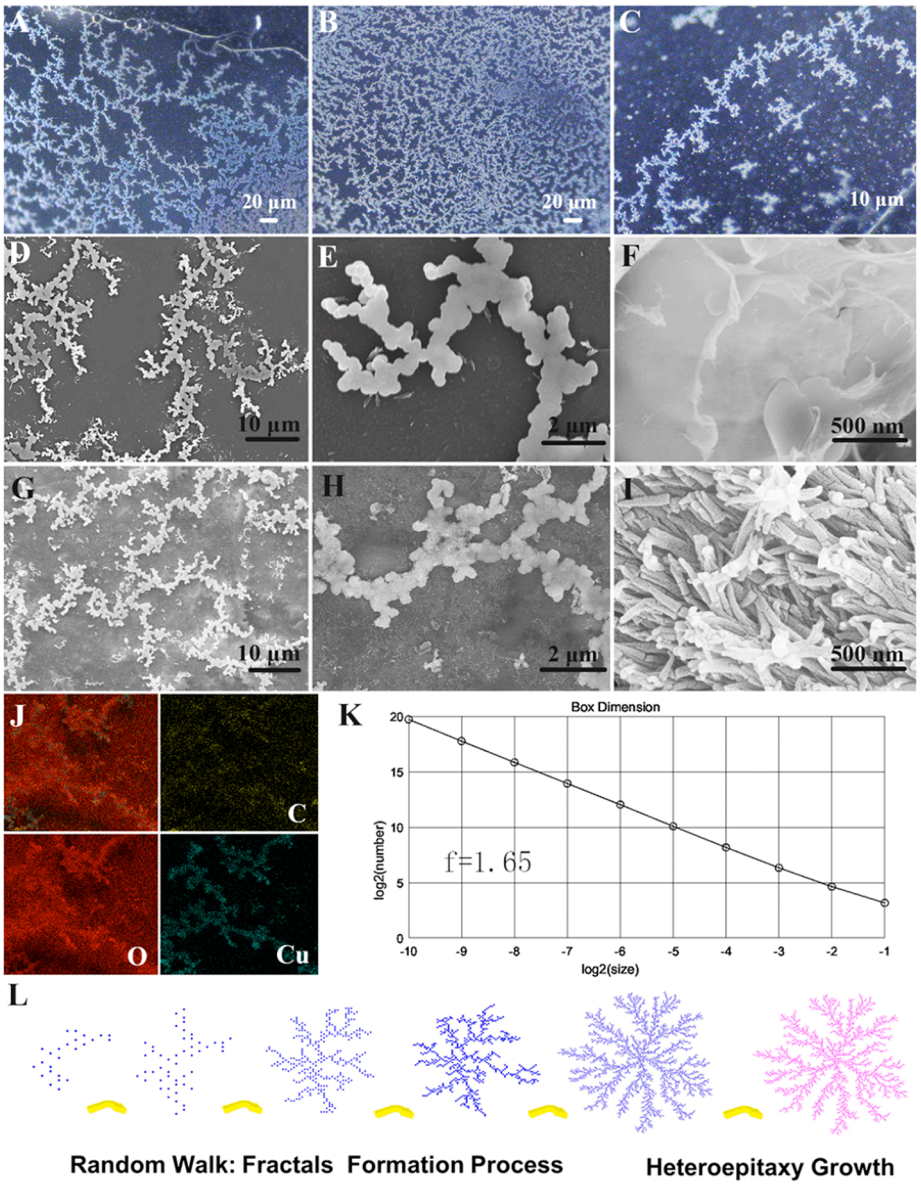

Figure 2. (A–C) OM figures of CP/Cu-CAT fractals. SEM figures of (D–F) CP/$Cu(OH)_2$ fractals. (G–I) CP/Cu-CAT fractals. (J) SEM mapping for CP/Cu-CAT fractals. (K) Fractal dimension calculation of the Cu-CAT fractals. (L) Fractals formation driven by random walk and heteroepitaxy growth.

$NH_3{\cdot}H_2O$ solution. After complete dissolution, the $Cu(NH_3)_4(OH)_2$ solution was achieved. Then the $Cu(NH_3)_4(OH)_2$ solution was dripped on the surface of CP at room temperature. During the evaporation and crystallization process, unstable $Cu(NH_3)_4(OH)_2$ decomposed. $Cu(OH)_2$ fractals pattern formed on CP when the slow evaporation finished, denoted as CP/$Cu(OH)_2$, as the precursor for synthesis of Cu-CAT. The next step was immersing the CP/$Cu(OH)_2$ in ethanol solution of 0.1 g of 2,3,6,7,10,11-hexahydroxytriphenylene ($H_{12}C_{18}O_6$, HHTP) for 1 h to finish heteroepitaxy self-assembly. The final obtained material was carefully washed and dried, denoted as CP/Cu-CAT fractals.

Electrochemical Measurement. Ag/AgCl, Pt, and samples, respectively, as reference electrode, counter electrode, and working electrode were assembled for a three-electrode system. Here, 0.1 M NaCl solution (pH = 5.5) is simulated sweat; $0.1–10^5$ Hz and 50 mV s^{-1} were set for the electrochemical impedance spectroscopy (EIS) test frequency and cyclic voltammetry (CV) scan rate for electrochemical behavior measurement, respectively. For the proton conductivity test, a quasi-four-probe electrochemical cell was carried out with an applied alternating current (AC) voltage of 100 mV and frequency of $1–10^6$ Hz. Potentials of −0.1 and +0.5 V were, respectively, set for lactate and glucose oxidation for the sensing performance test. For perspiration analysis, Zhengyun Wang as the first author of this paper was recruited as a healthy volunteer for sweat collection in this research. Also, informed consent was obtained from the individual. Two hours of continuous exercise with high intensity was done before the sweat collection. More details are included in the Supporting Information.

RESULTS AND DISCUSSION

Morphological and Structural Characterization. From the optical microscopy (OM) examination results in Figure 2A–C, it can be clearly observed that large-area, branched, and self-similar patterns of Cu-CAT are obtained on carbon paper (CP). Structures of fractals including precursor and MOFs are further characterized by field-emission scanning electron microscopy (FSEM), as shown in Figure 2D–I. Figure 2D exhibits the $Cu(OH)_2$ fractal precursor realized via random

DOI: 10.1021/acsami.9b11726
ACS Appl. Mater. Interfaces 2019, 11, 32310–32319

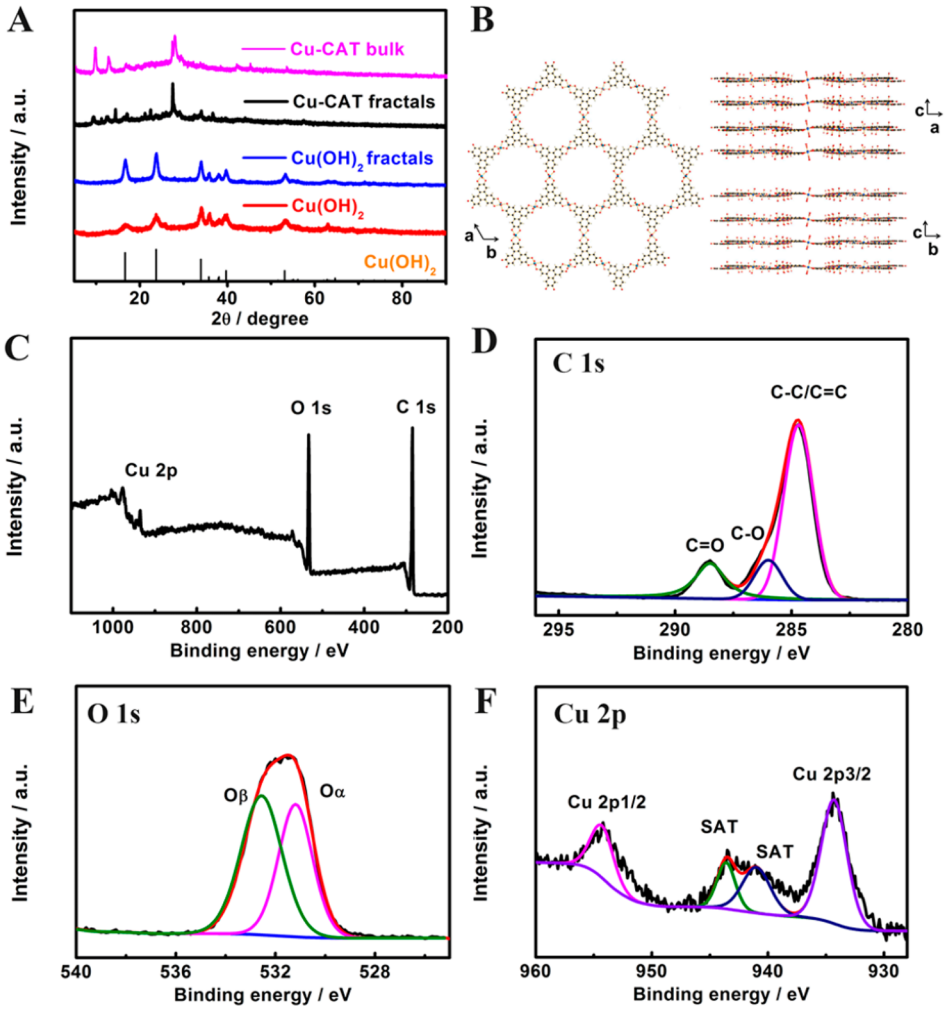

Figure 3. (A) XRD of $Cu(OH)_2$ before and after crystallization, Cu-CAT bulk and fractals. (B) Structure of Cu-CAT crystal. (C–F) XPS of Cu-CAT fractals.

walk, driven by evaporation of a $Cu(NH_3)_4(OH)_2$ drop. During this slow evaporation, large scale treelike architectures with many branches self-assemble on the surface of the CP. The higher magnification images (Figure 2E and F) reveal that the $Cu(OH)_2$ fractals are constructed from closely connected nanospheres with smooth surfaces. After immersing in HHTP solution for 1 h, the whole fractal patterns of MOFs are still maintained after heteroepitaxy growth, as displayed in Figure 2G and H. Figure 2I demonstrates that Cu-CAT fractals are composed of self-assembled uniform nanowires with well-defined dimensions, indicating the successful conversion from precursor to MOFs. The FSEM elementary mapping for C, O, and Cu also confirms the formation of Cu-CAT fractals (Figure 2J).

The fractal formation process is summarized: As the ammoniacal copper complex drop slowly evaporates, many initial nucleons generate. At the same time, a continuous "random walk" of $Cu(NH_3)_4(OH)_2$ drives it to preferentially attach to these nucleons. And then the mother branches gradually grow up along the initial nucleons. It is noted that $Cu(NH_3)_4(OH)_2$ as an unstable compound will lose NH_3 and completely transform into $Cu(OH)_2$ after crystallization. On the other hand, the energy barrier between two adjacent branches caused by charged $Cu(OH)_2$ will efficiently prevent other $Cu(OH)_2$ nanospheres from moving and arriving at the concave range produced by these two adjacent branches. Moreover, with evaporation proceeding, the distance between two adjacent branches gradually decreases, resulting in a decrease of the strength of the energy barrier. In other words, a critical distance exits. Once the $Cu(OH)_2$ nanospheres can break through the energy barrier and arrive at the concave region, a sub-branch would grow across the mother branch. The growth of the next generations of branches also follows this rule. Consequently, the branched and treelike fractal pattern spontaneously forms during the slow evaporation. For the heteroepitaxy growth, because Cu-CAT is crystallized with 21.36, 21.36, and 6.73 Å for *a*, *b*, and *c* crystallographic axes, respectively, and precursor $Cu(OH)_2$ has the close parameters of lattice match (2.95, 10.59, 5.26 Å for *a*, *b*, *c* axes, respectively), self-assembly occurs along the *a* and *c* axes of $Cu(OH)_2$, resulting in quasi-oriented conversion of Cu-CAT. Although different from the strict self-similarity at all scales of mathematical fractal such as Sierpinski's triangle, fractal Cu-CAT exhibits a distinctive boundary among treelike fractals due to cooperatively growth up from a central nucleus. Further, the fractal dimensionality has been counted by using the method of box counting in fractal theory (Figure 2K). The fractal dimensionality f of Cu-CAT is calculated as 1.65,

DOI: 10.1021/acsami.9b11726
ACS Appl. Mater. Interfaces 2019, 11, 32310–32319

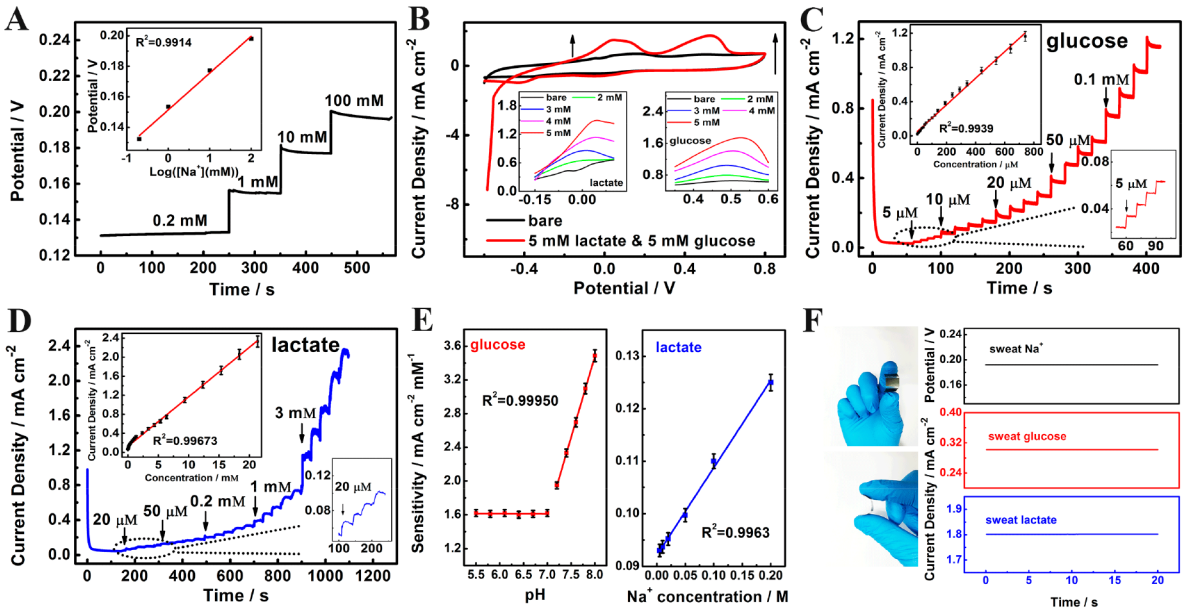

Figure 4. (A) Potentiometric response of CP/Cu-CAT fractals in NaCl solution with different concentrations. Inset is the corresponding calibration curve. (B) CV of CP/Cu-CAT fractals in simulated sweat (50 mVs^{-1}). Insets are CV (50 mV s^{-1}) responses to different concentrations of lactate and glucose. Current responses of CP/Cu-CAT fractals to consecutive additions of (C) glucose and (D) lactate in simulated sweat. Insets are the corresponding calibration curve. (E) Relationship between glucose sensitivity and pH; lactate sensitivity and C_{Na+}. (F) Photographs of CP/Cu-CAT fractals connected by transparent tape (left). Response to sweat Na^+, glucose, and lactate by using CP/Cu-CAT fractals (right).

demonstrating that the formation of the MOF fractals obeys DLA. The whole process can be simulated by running through the DLA mathematical program: first, an initial particle is set as the seed. Another particle generating at any position far from the seed walks randomly until it contacts the seed and becomes a part of the whole; second, a new particle randomly generates and the above process is repeated, leading to a large enough cluster, as shown in Figure 2L (see DLA code in the Supporting Information).

The typical X-ray diffraction (XRD) patterns of the different types of $Cu(OH)_2$ and Cu-CAT are shown in Figure 3A. The as-prepared $Cu(OH)_2$ for dissolving in ammonia−water exhibits diffraction peaks at 16.7°, 23.8°, 34.1°, 35.9°, 38.2°, 39.8°, and 53.2° corresponding to (020), (021), (002), (111), (022), (130), and (150) faces. The blue sample after recrystallization from ammonia−water shows the same patterns with the result of $Cu(OH)_2$ crystals, confirming that the crystalline product reverts to $Cu(OH)_2$. The data of MOF fractals and bulk verifies the crystals of Cu-CAT. These results fully confirm the successful conversion of Cu-CAT fractals from $Cu(OH)_2$. The structure of Cu-CAT crystals is shown in Figure 3B. Results of X-ray photoelectron spectroscopy (XPS) of Cu-CAT fractals are displayed in Figure 3C. The peaks of C 1s, O 1s, and Cu 2p are observed in Cu-CAT. The C 1s exhibits the peaks of the C═C/C−C (284.6 eV), C−O (286.5 eV), and C═O (288.3 eV) groups (Figure 3D). The O 1s spectrum of Cu-CAT is deconvoluted into two peaks denoted as O_α and O_β at 531.1 and 533.3 eV (Figure 3E). The peak O_α corresponds to the Cu−O bond, and O_β is associated with the carbon oxygen bond and hydroxyls. The two components of the Cu 2p peaks at 933.5 and 954.9 eV correspond to the Cu $2p_{3/2}$ and Cu $2p_{1/2}$ peaks of Cu-CAT fractals (Figure 3F). The other two peaks at 943.5 and 938.9 eV are assigned to satellite peaks. These results also verify the formation of Cu-CAT fractals.

Multiple Sensing Performances of CP/Cu-CAT Fractals and Sweat Analysis. Figure 4A presents the open-circuit potentials of CP/Cu-CAT fractals to Na^+ with concentrations of 0.2−100 mM. Surprisingly, a Nernstian-type response is observed when the sodium concentration increases. The potential shows a wide linear relationship with the logarithm of the Na^+ concentration with a high sensitivity 20 mV/dec (inset of Figure 4A). In contrast, bulk Cu-CAT does not show any response to Na^+ (Figure S13A). Thus, this newly discovered sodium ion sensing function is attributed to the fractal structure. Figure 4B summarizes the CV responses of CP/Cu-CAT fractals toward different concentrations of glucose and lactate in simulated perspiration (pH = 5.5). An interesting fact is that fractal structure endows the Cu-CAT MOFs with new capability to electro-oxidize glucose in acidic media. This also means that CP/Cu-CAT fractals can directly work in acidic sweat, unlike other copper-based materials which require alkaline conditions to detect glucose. CP/Cu-CAT fractals display two well-documented oxidation peaks corresponding to glucose and lactate oxidation. The oxidation peak current densities dramatically increase as respective concentrations increase, suggesting outstanding electrochemical catalytic activity of CP/Cu-CAT fractals. Furthermore, the current−time responses to glucose and lactate at the optimized potential are, respectively, presented in Figure 4C and D (see optimization in the Supporting Information, Figures S4−S11). With aliquot additions of analytes, the current densities of CP/Cu-CAT fractals gradually stepwise and steady-state current responses are obtained within 5 s. CP/Cu-CAT fractals demonstrate linear dynamic ranges from 0.005 to 0.74 mM for glucose and from 0.02 to 21.35 mM for lactate (insets of Figure 4C and D), with a high sensitivity of 1.62 mA cm^{-2} mM^{-1} and a detection limit down to 2.0 μM for glucose, and 0.11 mA cm^{-2} mM^{-1} and 10 μM for lactate, respectively (signal-to-noise ratio of 3). The lactate sensing performance of

DOI: 10.1021/acsami.9b11726
ACS Appl. Mater. Interfaces 2019, 11, 32310−32319

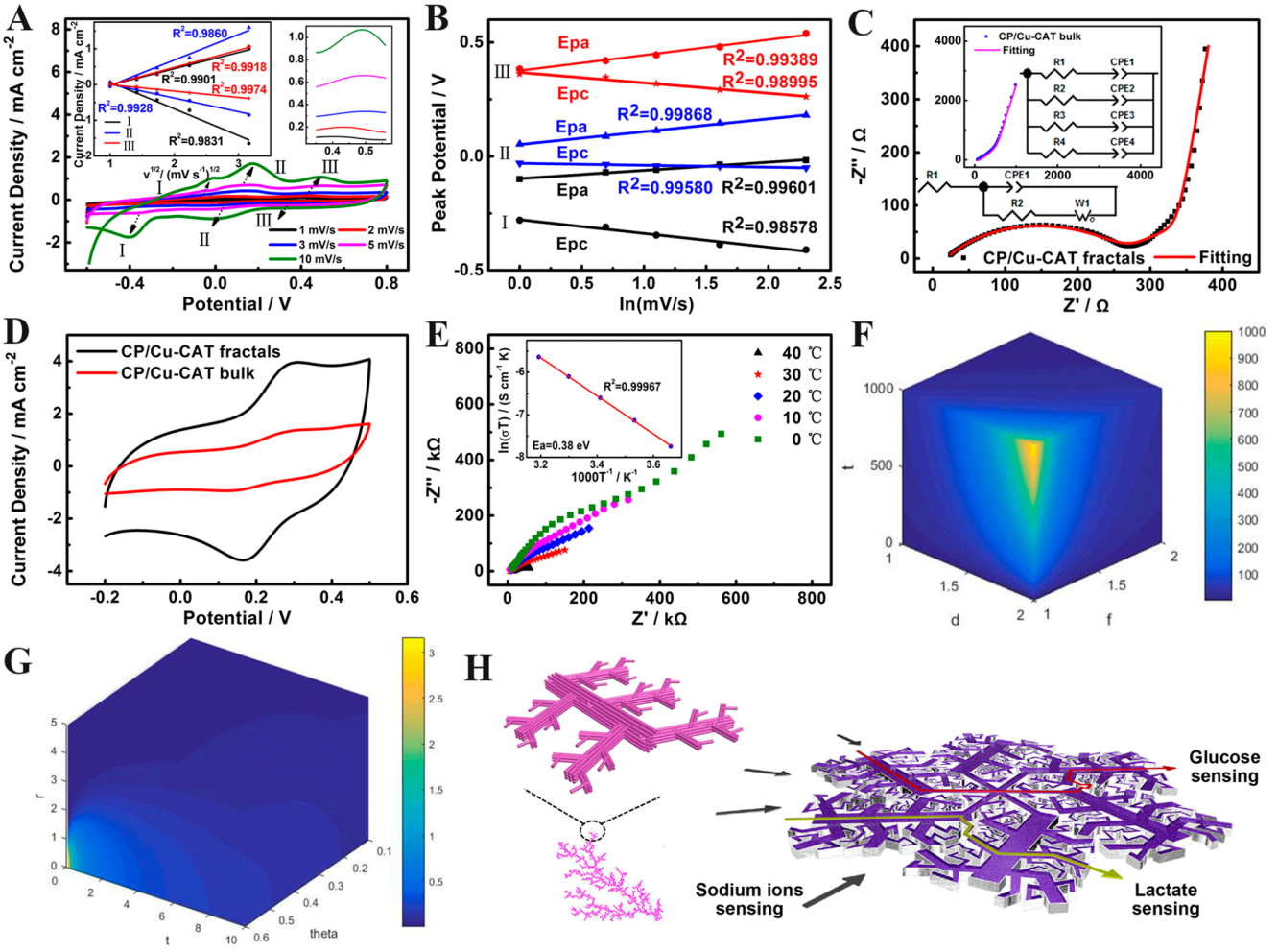

Figure 5. (A) CV of CP/Cu-CAT fractals in simulated sweat with 5.5 pH (0.1 M NaCl solution). Inset figures are peak of Cu(II)−Cu(III) and relationship between peak currents and square root of scan rates. (B) Corresponding linear relationship between peak potential and lnv. (C) Nyquist plots of CP/Cu-CAT fractals and bulk ($0.1-10^5$ Hz) in simulated sweat (pH = 5.5). (D) CV of CP/Cu-CAT fractals and bulk with $K_3Fe(CN)_6$ and $K_4Fe(CN)_6$ (both 1 mM) at 50 mV s^{-1}. (E) Nyquist plot of Cu-CAT from 0 to 150 °C and inset is corresponding Arrhenius plot of proton conductivities. (F) 4D-visualized function figure of $r(d, f, t)$. (G) 4D-visualized function figure of $p(r, t)$. (H) Cu-CAT fractal maze within different diffusion paths for analytes.

CP/Cu-CAT fractals is highly dependent on Na^+ concentration. Also, CP/Cu-CAT fractals exhibit excellent anti-interference ability, long-time stability, outstanding reproducibility, and flexibility (Figure S12). The sensing performances of CP/Cu-CAT fractals are comparable or superior to that of CP/Cu-CAT bulk and many reported electrochemical sensors based on other materials (Table S1). The sensing mechanisms of glucose and lactate are described:

For glucose:

$$\{Cu^{II}CAT\}_m + mH_2O \rightarrow \{Cu^{III}CAT{\cdot}OH\}_m + me^- \quad (1)$$

$$\frac{2}{m}\{Cu^{III}CAT{\cdot}OH\}_m + \text{glucose} \rightarrow \frac{2}{m}\{Cu^{II}CAT\}_m + \text{gluconolactone} \quad (2)$$

For lactate:

$$\{Cu^{II}CAT\}_m + mNa^+ + me^- \rightarrow \{Cu^{I}(Na^+)CAT\}_m \quad (3)$$

$$\{Cu^{I}(Na^+)CAT\}_m + \text{lactate} + 2Na^+ \rightarrow \{Cu^{I}{}_{1-2/m}(Cu^0)_{2/m}(Na^+)_{1+2/m}CAT\}_m + \text{pyruvate} \quad (4)$$

$$\{Cu^{I}{}_{1-2/m}(Cu^0)_{2/m}(Na^+)_{1+2/m}CAT\}_m \rightarrow \{Cu^{I}(Na^+)CAT\}_m + 2Na^+ + 2e^- \quad (5)$$

Figure 4E shows the relationship between glucose and lactate sensitivity and influencing ions, OH^- for glucose and Na^+ for lactate. It is remarkable that the sensitivity for glucose will not be influenced by the concentration of OH^- when the pH is less than 7, but will substantially enhance as the pH is more than 7. We speculate that this result is ascribed to the difference between the internal and external environment in MOF caused by its fractal structure (internal alkaline environment hypothesis). When the pH is less than 7, the oxidation of external Cu(II) is limited, and glucose oxidation would occur in the inter channels of Cu-CAT. The internal basic microenvironment would be kept relatively stable, making the glucose sensitivity free of external pH. But when

DOI: 10.1021/acsami.9b11726
ACS Appl. Mater. Interfaces 2019, 11, 32310−32319

the pH increases to more than 7, the external Cu(II) of Cu-CAT fractals will also be easily oxidized into Cu(III) besides the internal ones, resulting in the increase of glucose sensitivity. As for lactate, the occurrence of electron-hopping between adjacent redox centers in CP/Cu-CAT fractals accompanies the interfacial diffusion of sodium ions because of charge-balancing. As a result of this, the internal and external oxidized centers across the axis are exposed, which rapidly catalyzes lactate.

Motivated by the unique electrochemical performances of CP/Cu-CAT fractals, it is advisable to introduce the fractal MOFs into the sweat biosensor system as the multifunctional sensing element. For CP/Cu-CAT fractals, the sensing functions for Na^+, glucose, and lactate are independent of each other due to different sensing mechanisms. CP/Cu-CAT fractals can be utilized for direct acidic sweat testing without using any other auxiliary electrolyte. Here we use commercial transparent tape as the flexible substrate to connect CP/Cu-CAT fractals as the sensing array for selective screening of a panel of sodium ions, glucose and lactate in perspiration (Figure 4F). Before measurement, the pH of fresh sweat collected from the skin surface is measured as 5.5. In view of the static working manner in wearable sweat biosensors, the static measurement is performed to directly test perspiration without using simulated electrolyte for Na^+, glucose, and lactate responses. The potentials for glucose and lactate are operated at +0.5 and −0.1 V. From the current response toward glucose and lactate and the open-potential response toward Na^+ (Figure 4E), the concentration of sweat sodium ions, glucose, and lactate are, respectively, calculated as 31.6 mM, 159.1 μM, and 15.4 mM by using the calibration curves of the sensor signal versus stepwise-increased analyte concentration. In addition, this electrochemical method for sweat analysis has been compared with standard ultraviolet spectrophotometry. The results show that the electrochemical readout data by using CP/Cu-CAT fractals are accurate (see the Supporting Information).

Mechanism Analysis of Fractal Sensing. Based upon the discovery about electrochemical sensing performances of CP/Cu-CAT fractals, further efforts have been made to study electrochemical mechanism caused by fractals, especially for glucose and sodium ions sensing. CV with different scan rates is first employed to explore the electrochemical behavior of CP/Cu-CAT fractals, as displayed in Figure 5A. Three pairs of redox peaks at −0.02/−0.4, 0.18/−0.05, and 0.5/0.25 V (versus Ag/AgCl) correspond to interconversion of Cu(0)−Cu(I), Cu(I)−Cu(II), and Cu(II)−Cu(III) in 0.1 M NaCl solution (pH = 5.5). Generally, high hydroxide concentration in electrolyte dominates the oxidation of Cu(II) to Cu(III) at high potential, and thus, Cu(II) would not be oxidized into Cu(III) in acid conditions (Figure S18 in the Supporting Information). Nevertheless, we have observed the appearance of the Cu(II)−Cu(III) redox peak (peak III) for CP/Cu-CAT fractals in acid media. It is a fascinating electrochemical phenomenon. Redox peaks I, II, and III shift toward more positive and negative potentials, hinting at a quasi-reversible behavior. Also, the redox peak currents of peaks I, II, and III linearly increase with the square root of the scan rate, illustrating diffusion controlled processes (inset of Figure 5A). In the light of Laviron's theory,[39] we further calculated the electron transfer number (n) as well as electron transfer coefficient (α):

$$E_{pa} = E^0 + \frac{RT}{(1-\alpha)nF} + \frac{RT}{(1-\alpha)nF} \ln v \quad (6)$$

$$E_{pc} = E^0 + \frac{RT}{\alpha nF} - \frac{RT}{\alpha nF} \ln v \quad (7)$$

where temperature T (T = 298 K), Faraday constant F (96 500 C mol^{-1}), and gas constant R (8.314 J $mol^{-1}K^{-1}$) are known constants. Based upon the plots of peak potentials E_{pa} and E_{pc} versus the natural logarithm of the scan rate (ln v) (Figure 4B), α and n are, respectively, calculated to be 0.5 and 1, 0.86 and 1, and 0.60 and 1 for peaks I, II, and III, implying a single electron transfer process. When $n\Delta E_p$ > 200 mV, the electron transfer rate k_s can be achieved from the Laviron formula:[39]

$$k_s = \frac{\alpha nFv}{RT} \quad (8)$$

The k_s values for Cu(0)−Cu(I), Cu(I)−Cu(II), and Cu(II)−Cu(III) are, respectively, calculated as 0.19, 0.33, and 0.23 s^{-1} at 10 mV s^{-1}. Compared with the bulk MOFs (Figure S18A), this result implies fast electron transfer for copper conversion in Cu-CAT fractals, which facilitates glucose and lactate oxidation.

We further investigate the electrochemical reaction of redox peak Cu(II)−Cu(III) in acid media due to its critical effect in glucose sensing. Figure 5C compares EIS results of the CP/Cu-CAT fractals and bulk in 0.1 M NaCl solution at the setting potential of +0.5 V. Interestingly, CP/Cu-CAT fractals exhibit a semicircle and a line in the high and low frequency regions, respectively. The response at high and low frequency corresponds to the transport of charge in the Faraday reaction and the solid-state transport of charge carriers. The semicircle in the CP/Cu-CAT fractals corresponds to an interfacial electron transfer process, fully demonstrating the occurrence of electrochemical reaction, that is, the conversion from Cu(II) to Cu(III). The Faraday process for CP/Cu-CAT fractals including charge and mass transfer can be fitted and analyzed from the equivalent circuit (Figure S19 and Table S3). But CP supported bulk Cu-CAT exhibits a concave arc in the high frequency region and a line in the low frequency region, which is in accord with typical impedance spectra of double-layer supercapacitors (Figure S20). This result indicates only interfacial double-layer capacitance, instead of the process of electrochemical reaction for Cu-CAT bulk at high potential. It is also compliant with the result of CV of bulk Cu-CAT. The Cu-CAT bulk could be considered as a supercapacitor, which is composed of multiple horizontal RC ladder networks wired in parallel, as shown in the equivalent circuit. The EIS behavior difference between fractals and bulk reveals that conversion from Cu(II) to Cu(III) in acid media would occur in the interior of the Cu-CAT fractal structure, which confirms our speculation about internal alkaline environment hypothesis in Figure 4E.

In order to gain insights into the mechanism behind sensing using the fractal structure, the $[Fe(CN)_6]^{3-/4-}$ redox probe was used to calculate the electrochemical active surface areas (ECSAs) of CP/Cu-CAT fractals as well as CP supported bulk Cu-CAT. These two samples both display a pair of quasi-reversible single-electron redox peaks (Figure 5D). Reduced peak potential separation (E_p) and enhanced peak current (i_p) are obviously observed on CP/Cu-CAT fractals compared withCu-CATbulk, implying higher electrochemical activities. The reason is that the fractal structure provides many complex,

DOI: 10.1021/acsami.9b11726
ACS Appl. Mater. Interfaces 2019, 11, 32310−32319

hierarchical branches and maximized exposed surface in comparison with bulk morphology, enabling the superficial transport of substances and electrons with high efficiency. The EASAs of CP/Cu-CAT fractals and bulk are calculated as 26.0 and 9.1 cm^2 via the Randles−Sevcik formula, $i_p = 2.69 \times 10^5 n^{3/2} S D^{1/2} v^{1/2} c$ ($D = 6.3 \times 10^{-6}$ cm s^{-1}), manifesting that fractal structure plays a significant role in efficiently improving the ECSAs for the Cu-CAT MOFs. On the other hand, given the relevance between the proton transfer and observed electrochemical phenomenon, it is necessary to further investigate the proton conductions in Cu-CAT for analysis of this unique behavior. AC impedance measurements are performed by attaching copper-pasted electrodes to both identified sides of the Cu-CAT at different temperatures, to evaluate the proton conductions (Figure 5E). The proton conductivity σ (S cm^{-1}) of the Cu-CAT can be estimated based on the following equation:

$$\sigma = \frac{L}{SR} \tag{9}$$

$$\ln(\sigma T) = \ln A - \frac{Ea}{kT} \tag{10}$$

where k and A are the Boltzmann constant ($k = 1.381 \times 10^{-23}$ J K^{-1}) and the pre-exponential factor, respectively. The calculated value of 0.38 eV for E_a signifies that proton conduction in Cu-CAT belongs to the Grotthuss (hopping) mechanism (<0.4 eV), supporting that the strong hydrogen bonded network accompanied by $\pi-\pi$ interactions possesses the capability to facilitate efficient transfer of protons driven by chemical potential (see details in the Supporting Information).

On the basis of the above evaluation about CV, EIS, ECSAs, and proton transfer, a question emerges: Why do fractals enable Cu(II)−Cu(III) conversion for Cu-CAT in the acid media but bulk morphology cannot? The answer lies in subdiffusion caused by fractals. First, we might as well regard the MOF fractals as a maze and the proton as an ant. The process of protons diffusing in MOF fractals is analogous to that the ant takes random steps in the direction to neighboring sites in an infinite maze. Since in the fractal paths between connected neighboring sites have confined the diffusion, the conventional diffusion constant D_0 should be substituted with length-dependent diffusion $D(r)$.[40] The average mean square distance r that the ant moves in t time can be mapped onto the diffusion in Euclidean space:

$$D(r) = D_0 r^{-\theta} \quad (\theta > 0) \tag{11}$$

where θ is a constant. For average mean square distance r:

$$r^2(t) = D(r)t \tag{12}$$

Thus, the average mean square distance r can be achieved:

$$r^2(t) = (D_0{}^{2/2+\theta})(t^{2/2+\theta}) \tag{13}$$

Because the anomalous exponential $(2/(2+\theta))$ is less than 1, the diffusion in Cu-CAT fractals is subdiffusive (see the Supporting Information). Equation 13 can be rewritten as

$$r(t) = kt^{d/2f} \tag{14}$$

where d and f are the fracton dimensionality and fractal dimensionality of the diffusion medium ($d < f$). To intuitively observe the variation trend, the 4D-visualized function diagram for eq 14 has been simulated, as exhibited in Figure 5F. The color variation from blue to yellow manifests the variation of average mean square distance from short to long. The variable diffusion distance in the fractal structure is highly dependent on time, fracton dimensionality, and fractal dimensionality. Compared with the diffusion in Euclidean space, $r(t) = bt^{0.5}$, the distance in fractal media is less than that in Euclidean space in the same time, actually indicating that diffusion becomes more anomalous and slower in the fractal structure. It also illustrates that numerous branches create more detours for diffusion of hydrogen ions. Cu-CAT comprises a type of stacked layers. The copper coordinates to two adjacent deprotonated HHTP linkers and two water ligands.[41] For CP/Cu-CAT fractals, in the adjacent layers, the oxygen atoms of the HHTP are hydrogen bonded to the two axial water ligands that participate in the formation of these discrete complexes, which is a continuous hydrogen bonding network. Some protons at suitable positions in fractal MOFs will be combined with the oxygen atoms of the linker in MOFs and be transferred with the help of hydrogen bonding network. Benefiting from the "deadband" in fractal structures with high ECSAs, the whole diffusion of protons is slow and uneven, and other protons cannot transfer "in time". This leads to the creation of a relative basic microenvironment in some inter channels of MOFs. The basic microenvironment will be propitious to the oxidation of the internal Cu(II) of MOFs. For Cu-CAT bulk, the diffusion is normal because all the nanochannels are equivalent for transfer.

As for sodium ion sensing, it ascribes to a complicated process. We call this the "branch edge effect", induced by fractals. Cu-CAT fractals can be regarded as the combination of a sodium ion-selective membrane and ion-to-electron transducer, which causes the Nernstian response. On the fractal surface, stacking of 2D honeycomb grids in Cu-CAT MOFs gives rise to concave areas of uncoordinated oxygen. The unsaturated O-edge of the fractal would play an extremely significant role in the sodium ionophore; that is, the Na^+ hydrates can be bound by four noncovalent bonding interactions to the corresponding four oxygen atoms due to the structure match. Many hierarchical branches of fractals bring more particular sites for immobilization of Na^+ hydrates. More importantly, complicated surface textures of fractals remarkably improve accessibility during immobilization, resulting in stabilizing sodium ions with high efficiency. On the other hand, fractal assemblies consisting of oriented Cu-CAT nanowires would facilitate the electron transfer and enhance capacitance. Thus, Cu-CAT fractals also can serve as an ion-to-electron transducer, providing the capacitive coupling in the interior. But for the bulk surface, copper-edge or oxygen-edge exposure is completely random, making it difficult to stabilize Na^+ hydrates.

A theoretical model fractal maze has been introduced to better understand the sensing characteristics of Cu-CAT fractal structure. $p(r,t)$ is defined as the average probability of analytes per site at time t. For glucose and lactate sensing, according to the fractal diffusion theory:[42]

$$\frac{\partial p(r,t)}{\partial t} = \frac{D_0}{r^{f-1}} \frac{\partial}{\partial r}\left[r^{f-1-\theta} \frac{\partial p(r,t)}{\partial t} \right] \tag{15}$$

The solution of the equation is

DOI: 10.1021/acsami.9b11726
ACS Appl. Mater. Interfaces 2019, 11, 32310−32319

$$p(r, t) = \frac{2+\theta}{f\tau\left(\frac{f}{2+\theta}\right)}\left[\frac{1}{D_0(2+\theta)^2 t}\right]^{f/2+\theta} \exp\left[-\frac{r^{2+\theta}}{D_0(2+\theta)^2 t}\right] \quad (16)$$

where the fractal dimension f is 1.65 as mentioned above and τ as well as standard diffusion coefficients D_0 are constants. The exponent of anomalous diffusion θ is different for glucose and lactate as well as their catalytic products. Therefore, $p(r,t)$ can be regarded as the function of r, t, and θ. As exhibited in Figure 5G, visual color variation represents the probability density variation, fully demonstrating the different favorable diffusion path for glucose, lactate, and their catalytic products in Cu-CAT fractals maze. These specific paths would facilitate the diffusion and exchange of reactant and products (Figure 5H), which is beneficial to the enhancement of sensitivity and anti-interference ability, and thus can be suitable for sweat sensing. On the other hand, for CP/Cu-CAT fractals that have already been demonstrated toward ions and metabolites, further work for sweat sensing is needed to design more robust and stable mechanical components to provide reliable, actionable data for long-term use. To ensure safe handling of data, it is essential to incorporate microfluidics and multiplexed sensing to improve data integrity. Parallel efforts are needed including higher level investigation into the physiological relevance of sweat analytes through large-scale correlation studies.

CONCLUSION

In summary, the fractal design has been creatively proposed for the first time for directing diffusion limited aggregates of metal hydroxide toward MOF fractals inspired from salt water evaporation, a phenomenon in our life. It has been shown that the MOF fractals would form through two steps of self-assembly, evaporation-driven random walk and heteroepitaxy growth. We have discovered that MOF fractals exhibit unique property of subdiffusion and edge effect, which would play a prominent role in electrochemical sweat sensing, especially glucose determination in acid media and sodium ions response. With such a property, the as-prepared CP/Cu-CAT fractals can function as a versatile biosensor for sweat sodium ion, glucose, and lactate monitoring. Fractals bring a new way of perceiving and open an amazing horizon for MOF investigation including self-assembly, unusual physicochemical properties, and new functions. It is envisioned that the fractal strategy will pave the way for new generation of MOF-based sweat biosensors and broaden the avenue of designing novel functional materials. More amazing phenomena and unique properties of fractal materials await discovery, exploration, and sophisticated theoretical analysis at different scales.

ASSOCIATED CONTENT

Supporting Information

The Supporting Information is available free of charge on the ACS Publications website at DOI: 10.1021/acsami.9b11726.

Preparation and test details, material characterization, optimization of conditions for lactate and detection, sensing performances of reported analogue electrochemical biosensors, procedures of sweat test, ultraviolet spectrophotometry validating, electrochemical performances comparison, CV of CP/Cu-CAT bulk and copper sheet, results of EIS fitting, calculation about E_a, deduction about subdiffusion, DLA code (PDF)

AUTHOR INFORMATION

Corresponding Author

*E-mail: liuhf@hust.edu.cn.

ORCID

Fei Xiao: 0000-0002-7081-1998

Hongfang Liu: 0000-0001-5012-7278

Author Contributions

All authors have given approval to the final version of the manuscript.

Funding

This research is supported by National Natural Science Foundation of China (U1662114), National Key Research and Development Program of China (2018YFF0215002), the Foundation of Hubei Key Laboratory of Material Chemistry and Service Failure (No. 201502, 201702), the Independent Innovation Research Fund of Huazhong University of Science and Technology (2017KFYXJJ164), Key Laboratory of Material Chemistry for Energy Conversion and Storage, Ministry of Education (2018).

Notes

The authors declare no competing financial interest.

ACKNOWLEDGMENTS

We thank all the funding for supporting this work.

REFERENCES

(1) Sanchez, C.; Arribart, H.; Giraud Guille, M. M. Biomimetism and Bioinspiration as Tools for the Design of Innovative Materials and Systems. *Nat. Mater.* **2005**, *4*, 277−288.

(2) Aizenberg, J.; Weaver, J. C.; Thanawala, M. S.; Sundar, V. C.; Morse, D. E.; Fratzl, P. Skeleton of *Euplectella* sp.: Structural Hierarchy from the Nanoscale to the Macroscale. *Science* **2005**, *309*, 275−278.

(3) Liu, K.; Jiang, L. Bio-Inspired Design of Multiscale Structures for Function Integration. *Nano Today* **2011**, *6*, 155−175.

(4) Trogadas, P.; Cho, J. I. S.; Neville, T. P.; Marquis, J.; Wu, B.; Brett, D. J. L.; Coppens, M. O. A Lung-Inspired Approach to Scalable and Robust Fuel Cell Design. *Energy Environ. Sci.* **2018**, *11*, 136−143.

(5) Bassett, D. S.; Meyer-Lindenberg, A.; Achard, S.; Duke, T.; Bullmore, E. Adaptive Reconfiguration of Fractal Small-World Human Brain Functional Networks. *Proc. Natl. Acad. Sci. U. S. A.* **2006**, *103*, 19518−19523.

(6) Mandelbrot, B. B.; Wheeler, J. A. The Fractal Geometry of Nature. *Am. J. Phys.* **1983**, *51*, 286−287.

(7) Barnsley, M. F. *Fractals Everywhere*, Second ed.; Academic Press, 1993; pp XIII−XIV.

(8) Kempkes, S. N.; Slot, M. R.; Freeney, S. E.; Zevenhuizen, S. J. M.; Vanmaekelbergh, D.; Swart, I.; Smith, C. M. Design and Characterization of Electrons in a Fractal Geometry. *Nat. Phys.* **2019**, *15*, 127−131.

(9) Shang, J.; Wang, Y.; Chen, M.; Dai, J.; Zhou, X.; Kuttner, J.; Hilt, G.; Shao, X.; Gottfried, J. M.; Wu, K. Assembling Molecular Sierpiński Triangle Fractals. *Nat. Chem.* **2015**, *7*, 389−393.

(10) Wang, L.; Liu, R.; Gu, J.; Song, B.; Wang, H.; Jiang, X.; Zhang, K.; Han, X.; Hao, X.-Q.; Bai, S.; Wang, M.; Li, X.; Xu, B.; Li, X. Self-Assembly of Supramolecular Fractals from Generation 1 to 5. *J. Am. Chem. Soc.* **2018**, *140*, 14087−14096.

(11) Zhang, X.; Li, N.; Gu, G.-C.; Wang, H.; Nieckarz, D.; Szabelski, P.; He, Y.; Wang, Y.; Xie, C.; Shen, Z.-Y.; Lü, J.-T.; Tang, H.; Peng, L.-M.; Hou, S.-M.; Wu, K.; Wang, Y.-F. Controlling Molecular Growth between Fractals and Crystals on Surfaces. *ACS Nano* **2015**, *9*, 11909−11915.

(12) Xu, L.; Gutbrod, S. R.; Ma, Y.; Petrossians, A.; Liu, Y.; Webb, R. C.; Fan, J. A.; Yang, Z.; Xu, R.; Whalen, J. J., III; Weiland, J. D.; Huang, Y.; Efimov, I. R.; Rogers, J. A. Membranes: Materials and

Fractal Designs for 3D Multifunctional Integumentary Membranes with Capabilities in Cardiac Electrotherapy. *Adv. Mater.* **2015**, *27*, 1731−1737.
(13) Young, I. D.; Fraser, J. S. Biomaterials in Non-Integer Dimensions. *Nat. Chem.* **2019**, *11*, 599−600.
(14) James, S.; Contractor, R. Study on Nature-Inspired Fractal Design-Based Flexible Counter Electrodes for Dye-Sensitized Solar Cells Fabricated using Additive Manufacturing. *Sci. Rep.* **2018**, *8*, 17032.
(15) Zheng, X.; Shen, G.; Wang, C.; Li, Y.; Dunphy, D.; Hasan, T.; Brinker, C. J.; Su, B.-L. Bio-Inspired Murray Materials for Mass Transfer and Activity. *Nat. Commun.* **2017**, *8*, 14921.
(16) Wang, Z.; Liu, T.; Yu, Y.; Asif, M.; Xu, N.; Xiao, F.; Liu, H. Coffee Ring-Inspired Approach toward Oriented Self-Assembly of Biomimetic Murray MOFs as Sweat Biosensor. *Small* **2018**, *14*, 1802670.
(17) Wang, Z.; Liu, T.; Asif, M.; Yu, Y.; Wang, W.; Wang, H.; Xiao, F.; Liu, H. Rimelike Structure-Inspired Approach toward in Situ-Oriented Self-Assembly of Hierarchical Porous MOF Films as a Sweat Biosensor. *ACS Appl. Mater. Interfaces* **2018**, *10*, 27936−27946.
(18) Ma, T.; Gao, H.-L.; Cong, H.-P.; Yao, H.-B.; Wu, L.; Yu, Z.-Y.; Chen, S.-M.; Yu, S.-H. A Bioinspired Interface Design for Improving the Strength and Electrical Conductivity of Graphene-Based Fibers. *Adv. Mater.* **2018**, *30*, 1706435.
(19) Stassen, I.; Burtch, N.; Talin, A.; Falcaro, P.; Allendorf, M.; Ameloot, R. An Updated Roadmap for the Integration of Metal-Organic Frameworks with Electronic Devices and Chemical Sensors. *Chem. Soc. Rev.* **2017**, *46*, 3185−3241.
(20) Adil, K.; Belmabkhout, Y.; Pillai, R. S.; Cadiau, A.; Bhatt, P. M.; Assen, A. H.; Maurin, G.; Eddaoudi, M. Gas/Vapour Separation Using Ultra-Microporous Metal-Organic Frameworks: Insights into the Structure/Separation Relationship. *Chem. Soc. Rev.* **2017**, *46*, 3402−3430.
(21) Doonan, C.; Riccò, R.; Liang, K.; Bradshaw, D.; Falcaro, P. Metal-Organic Frameworks at the Biointerface: Synthetic Strategies and Applications. *Acc. Chem. Res.* **2017**, *50*, 1423−1432.
(22) Wang, T.; Jin, R.; Wu, Y.; Zheng, J.; Li, X. Chemical Induced Fragmentation of MOFs for Highly Efficient Ni-Based Hydrogen Evolution Catalysts. *Nanoscale Horiz* **2018**, *3*, 218−225.
(23) Liu, J.; Wöll, C. Surface-Supported Metal-Organic Framework Thin Films: Fabrication Methods, Applications, and Challenges. *Chem. Soc. Rev.* **2017**, *46*, 5730−5770.
(24) Rubio-Martinez, M.; Avci-Camur, C.; Thornton, A. W.; Imaz, I.; Maspoch, D.; Hill, M. R. New Synthetic Routes towards MOF Production at Scale. *Chem. Soc. Rev.* **2017**, *46*, 3453−3480.
(25) Wang, Z.; Gui, M.; Asif, M.; Yu, Y.; Dong, S.; Wang, H.; Wang, W.; Wang, F.; Xiao, F.; Liu, H. A Facile Modular Approach to the 2D Oriented Assembly MOF Electrode for Non-Enzymatic Sweat Biosensors. *Nanoscale* **2018**, *10*, 6629−6638.
(26) Shekhah, O.; Fu, L.; Sougrat, R.; Belmabkhout, Y.; Cairns, A. J.; Giannelis, E. P.; Eddaoudi, M. Successful Implementation of the Stepwise Layer-by-Layer Growth of MOF Thin Films on Confined Surfaces: Mesoporous Silica Foam as a First Case Study. *Chem. Commun.* **2012**, *48*, 11434−11436.
(27) Li, W.-J.; Tu, M.; Cao, R.; Fischer, R. A. Metal-Organic Framework Thin Films: Electrochemical Fabrication Techniques and Corresponding Applications &Perspectives. *J. Mater. Chem. A* **2016**, *4*, 12356−12369.
(28) Rodenas, T.; Luz, I.; Prieto, G.; Seoane, B.; Miro, H.; Corma, A.; Kapteijn, F.; Llabrés i Xamena, F. X.; Gascon, J. Metal-Organic Framework Nanosheets in Polymer Composite Materials for Gas Separation. *Nat. Mater.* **2015**, *14*, 48−55.
(29) Yoo, Y.; Jeong, H.-K. Rapid Fabrication of Metal Organic Framework Thin Films Using Microwave-Induced Thermal Deposition. *Chem. Commun.* **2008**, *21*, 2441−2443.
(30) Biemmi, E.; Scherb, C.; Bein, T. Oriented Growth of the Metal Organic Framework $Cu_3(BTC)_2(H_2O)_3{\cdot}xH_2O$ Tunable with Functionalized Self-Assembled Monolayers. *J. Am. Chem. Soc.* **2007**, *129*, 8054−8055.
(31) Schoedel, A.; Scherb, C.; Bein, T. Oriented Nanoscale Films of Metal-Organic Frameworks By Room-Temperature Gel-Layer Synthesis. *Angew. Chem.* **2010**, *122*, 7383−7386.
(32) Crivoi, A.; Duan, F. Evaporation-Induced Branched Structures from Sessile Nanofluid Droplets. *J. Phys. Chem. C* **2013**, *117*, 7835−7843.
(33) Bariya, M.; Nyein, H. Y. Y.; Javey, A. Wearable Sweat Sensors. *Nat. Electron.* **2018**, *1*, 160−171.
(34) Gao, W.; Emaminejad, S.; Nyein, H. Y. Y.; Challa, S.; Chen, K.; Peck, A.; Fahad, H. M.; Ota, H.; Shiraki, H.; Kiriya, D.; Lien, D.-H.; Brooks, G. A.; Davis, R. W.; Javey, A. Fully Integrated Wearable Sensor Arrays for Multiplexed in Situ Perspiration Analysis. *Nature* **2016**, *529*, 509−514.
(35) Wang, Z.; Dong, S.; Gui, M.; Asif, M.; Wang, W.; Wang, F.; Liu, H. Graphene Paper Supported MoS_2Nanocrystals Monolayer with Cu Submicron-Buds: High-Performance Flexible Platform for Sensing in Sweat. *Anal. Biochem.* **2018**, *543*, 82−89.
(36) Bandodkar, A. J.; Molinnus, D.; Mirza, O.; Guinovart, T.; Windmiller, J. R.; Valdés-Ramírez, G.; Andrade, F. J.; Schöning, M. J.; Wang, J. Epidermal Tattoo Potentiometric Sodium Sensors with Wireless Signal Transduction for Continuous Non-Invasive Sweat Monitoring. *Biosens. Bioelectron.* **2014**, *54*, 603−609.
(37) Talary, M. S.; Dewarrat, F.; Huber, D.; Caduff, A. In Vivo Life Sign Application of Dielectric Spectroscopy and Non-Invasive Glucose Monitoring. *J. Non-Cryst. Solids* **2007**, *353*, 4515−4517.
(38) Derbyshire, P. J.; Barr, H.; Davis, F.; Higson, S. P. J. Lactate in Human Sweat: a Critical Review of Research to the Present Day. *J. Physiol. Sci.* **2012**, *62*, 429−440.
(39) Laviron, E. General Expression of the Linear Potential Sweep Voltammogram in the Case of Diffusionless Electrochemical Systems. *J. Electroanal. Chem. Interfacial Electrochem.* **1979**, *101*, 19−28.
(40) Gefen, Y.; Aharony, A.; Alexander, S. Anomalous Diffusion on Percolating Clusters. *Phys. Rev. Lett.* **1983**, *50*, 77−80.
(41) Hmadeh, M.; Lu, Z.; Liu, Z.; Gándara, F.; Furukawa, H.; Wan, S.; Augustyn, V.; Chang, R.; Liao, L.; Zhou, F.; Perre, E.; Ozolins, V.; Suenaga, K.; Duan, X.; Dunn, B.; Yamamto, Y.; Terasaki, O.; Yaghi, O. M. New Porous Crystals of Extended Metal-Catecholates. *Chem. Mater.* **2012**, *24*, 3511−3513.
(42) Metzler, R.; Glöckle, W. G.; Nonnenmacher, T. F. Fractional Model Equation for Anomalous Diffusion. *Phys. A* **1994**, *211*, 13−24.

DOI: 10.1021/acsami.9b11726
ACS Appl. Mater. Interfaces 2019, 11, 32310−32319